FREE SURFACE FLOW AND WAVE IMPACT
AT COMPLEX SOLID STRUCTRES

Robert Mayon[1, 3]*, Zoheir Sabeur[2, 1], Tan Mingyi[3], Kamal Djidjeli[4]

[1]Southampton Marine and Maritime Institute, University of Southampton, UK
E-mail: r.mayon@soton.ac.uk

[2]IT Innovation Centre, Electronics and Computer Science,
Faculty of Physical Science and Engineering, University of Southampton, UK
E-mail: zas@it-innovation.soton.ac.uk

[3]Fluid Structure Interaction Group,
Faculty of Engineering and the Environment, University of Southampton, UK
E-mail: m.tan@soton.ac.uk

[4]Computational Engineering and Design Group,
Faculty of Engineering and the Environment, University of Southampton, UK
E-mail: kkd@soton.ac.uk

* Corresponding Author

ABSTRACT

Hydrodynamic wave loading at structures is a complex phenomenon to quantify. The design of structures to resist wave loading has been historically and predominantly achieved through empirical and experimental observations. This is due to the challenging understanding and quantification of wave impact energy transfer processes with air entrainment at solid structures. This paper investigates wave loading on such structures with effects of air entrapment. Specifically, it focuses on predicting the multi-modal oscillatory wave impact pressure signals which result from transient waves impinging upon a solid wall. A large dataset of compressible (and incompressible) numerical modelling scenarios have been generated to investigate these processes. The modelling simulation data are verified through a grid scaling analysis and validated against previous studies. Air bubble entrapment oscillatory pressure response trends are observed in the compressible simulation during wave impact. A frequency domain analysis of the impact pressure response is undertaken. The numerical modelling results are found in good agreement with theoretical and experimental observation data. These findings provide good confidence on the robustness of our numerical model foundations particularly for investigating the air bubbles formation, their mechanics and adjusted resonance frequency modes at impact with solid walls.

1. INTRODUCTION

Severe damage can be inflicted on coastal defence structures as a result of high intensity wave forces. Many laboratory experiments have been performed to gain an understanding of the physical processes which occur at the wave impact interface, see e.g. [1], [2], [3], [4]. The damage sustained by coastal defences is often caused by their continuous exposure to transient wave impact pressures which at the present time are not fully understood, e.g. [5], [6], [7]. Additionally, pulse-like oscillatory pressure signals have been observed in many experimental studies, [8], [9], [10], [11]. These oscillations manifest themselves subsequent to the initial wave impact with solid walls and may be a source of much serious damage and deterioration to the structural integrity of coastal defences. Experimental studies for the validation of these oscillatory impact pressure response results has proven to be very difficult because of the highly nonlinear, transient nature of the wave breaking process, [12]. This has led researchers to

speculate as to the source of the observed oscillations within the pressure response signal. In this study we analyse the impact of a solitary wave with a solid interface while employing a CFD approach. Experimental work has shown that incident waves on vertical structures can produce impulse pressures which greatly exceed magnitudes of the typical pressures that are expected when employing shallow water wave theory methods for analysis, [10]. The magnitude of these impulse pressures can commonly exceed:

$$10\rho g(h + H) \tag{1}$$

H is the wave height, *h* is the water depth, ρ the water density and g the acceleration due to gravity. These higher magnitude impulse pressures have been attributed to a phenomenon often termed as the wave 'flip-through' effect, [10]. However, additional highly destructive oscillatory pressure effects have been observed in experimental studies. These usually occur when air bubbles are entrained at impact. In this instance, the entrapped air bubbles will compress and dilate with a range of specific oscillatory frequencies. Further, and according to past theoretical, [13] and experimental studies, [9], the frequency range with which these bubbles oscillate will be dependent on the size of the entrained air void during their formation.

In this paper, we briefly introduce the theory of free surface fluid flow; and the numerical methods to simulate wave impact at solid structures. We also introduce theories and experiments from the literature which show the relationships between formed sizes of air bubbles in fluid flows and their typical resonance frequencies of oscillation. We investigate numerical dam-break flow simulations with impact at a solid vertical wall and air entrapment. Specifically, the collapsing water column propagates across the model domain and impacts a solid interface. The initial simulation case of a two-phase incompressible flow is described. Our model is then modified to simulate compressible flow case. A large data set of test cases was generated by employing first and second order equation discretisation schemes for both the temporal and spatial terms in the fluid flow governing equations. A range of grid resolutions were also applied to the model to ensure veracity of results.

2. FREE SURFACE FLOW AND BUBBLE OSCILLATION THEORIES

2.1 Numerical Methods

The numerical simulations were preformed using the finite volume technique based open source CFD code OpenFOAM, [14]. This software is compiled as a collection of C++ libraries with dedicated pre-programmed solvers which can be used to model various fluid flow simulation scenarios. In this study, the incompressible two-phase solver `InterFoam` was first used to analyse the flow field development. Subsequently, the `compressibleInterFoam` solver was used to examine the effects of air entrapment in the fluid phase during wave breaking. Both of these solvers use the phase fraction based Volume of Fluid method (VOF), [15], to capture and represent the interface between the two fluids.

2.1.1 Volume of fluid method

The interaction of the individual fluid phase constituents in the model is important as the pressure transfer across the free surface boundary which defines an entrained air bubble is central to this study. In the volume of fluid method a function $\alpha(x, y, t)$, is introduced at each grid cell in the model domain. The value of this function is defined as unity at any cell which is fully occupied by the fluid; and zero at any cell completely devoid of fluid. Cells with intermediate values may contain a droplet, a bubble or are located such that the interface between the two fluids intersects that cell. In the VOF method, the temporal evolution of the phase fraction function and thus the advection of the flow in two dimensional space is governed by the following transport equation:

$$\frac{\partial \alpha}{\partial t} + u\frac{\partial \alpha}{\partial x} + v\frac{\partial \alpha}{\partial y} = 0 \tag{2}$$

Where the phase volume fraction $\alpha \in [0,1]$, and *u* and *v* are the fluid velocities in the *x* and *y* direction respectively. By calculating the derivatives of the α function at each cell boundary the free surface normal can be established, [16]. The normal direction to the free surface is then the direction in which the α function varies most rapidly (i.e.$\nabla \alpha$). From the value of the α function and the direction of the

normal to the fluid interface, a line cutting the cell can be drawn which represents the free surface boundary.

2.1.2 Incompressible model governing equations
The conservation of mass equation for an incompressible fluid is defined as follows:

$$\nabla \cdot \boldsymbol{U} = 0 \tag{3}$$

And the conservation of mass equation for the volume fraction $\alpha \in [0,1]$ can be represented as:

$$\frac{\partial \alpha}{\partial t} + \nabla \cdot \boldsymbol{U}\alpha + \nabla \cdot \boldsymbol{U}_c\alpha(1-\alpha) = 0 \tag{4}$$

Where $\boldsymbol{U}$ is the fluid velocity vector, and $\boldsymbol{U}_c$ is the artificial compression velocity vector given by $\boldsymbol{U}_c = \min[\boldsymbol{U}, \max(\boldsymbol{U})]$. The final term on the left hand side ensures a sharp interface is maintained between the fluid phases. The momentum conservation equation is formulated by summing the averaged fluid properties according to their constituent proportion in the boundary cell. For a two phase flow, density ρ in the cells is given by:

$$\rho = \sum_{\alpha=1}^{2} r_\alpha \rho_\alpha \tag{5}$$

Where r_α is the volumetric fraction of each constituent fluid in the free surface boundary cell.
A single momentum conservation equation for an incompressible fluid can then be defined for the homogeneous mixture as:

$$\frac{\partial(\rho\boldsymbol{U})}{\partial t} + \nabla \cdot (\rho\boldsymbol{U}\boldsymbol{U}) = -\nabla p_h + \nabla \cdot \mu(\nabla\boldsymbol{U} + \nabla\boldsymbol{U}^T) + \boldsymbol{F}_s + \rho\boldsymbol{f}_i \tag{6}$$

Where ρ is given in Equation (5), p_h is the hydrostatic pressure, μ is the fluid viscosity and $\boldsymbol{f}_i$ is the gravitational force. The term $\boldsymbol{F}_s$ represents the surface tension force and is calculated from $\boldsymbol{F}_s = \sigma\kappa\nabla\alpha$, where σ is the interfacial tension and the interface curvature is given by $\kappa = \nabla \cdot (\nabla\alpha/|\nabla\alpha|)$.

2.1.3 Compressible model equations
To include the effects of compressibility within the model an Equation of State (EOS) must be defined for each phase. For the air phase, the ideal gas EOS is specified as follows:

$$\rho_a = p\frac{1}{R_a T} \tag{7}$$

Where ρ_a is the air density, R_a is the specific gas constant for air, T is the air temperature and p is the pressure. For the water phase the perfect fluid EOS is defined as:

$$\rho_W = p\frac{1}{R_W T} + \rho_{W0} \tag{8}$$

Where ρ_{W0} represents the density of water at atmospheric pressure conditions. An additional term must be incorporated into equation (4) in order to allow for air to be modelled as a compressible medium in the interfacial cells.

$$\frac{\partial \alpha}{\partial t} + \nabla \cdot \boldsymbol{U}\alpha + \nabla \cdot \boldsymbol{U}_c\alpha(1-\alpha) = -\frac{\alpha}{\rho_W}\frac{\mathrm{D}\rho_W}{\mathrm{D}t} \tag{9}$$

The Euler compressible mass conservation equation is defined as:

$$\frac{\partial \rho}{\partial t} + \nabla \cdot (\rho\boldsymbol{U}) = 0 \tag{10}$$

The transport equation for the temperature term is derived from the energy conservation equation, [17] and is calculated accordingly using equation (11) below:

$$\frac{\partial \rho T}{\partial t} + \nabla \cdot (\rho \boldsymbol{U} T) - \Delta(\mu T) = -\left(\frac{\alpha}{C_w} + \frac{1-\alpha}{C_a}\right)\left(\frac{\partial \rho k}{\partial t} + \nabla \cdot (\rho \boldsymbol{U} k) + \nabla \cdot (\boldsymbol{U} p)\right) \qquad (11)$$

C_w and C_a are the specific heat capacities for water and air respectively, while k is the specific kinetic energy. A flow field solution can be obtained by applying the PIMPLE algorithm which is a pressure-velocity coupling approach derived through combining the PISO and SIMPLE algorithms.

2.2 Resonant Oscillation Frequency of a Single Bubble
2.2.1 Analytical method
The behaviour of a single air bubble which is entrained within an infinite water domain has previously been studied by Minnaert [13]. An analytic expression describing the resonant frequency of a bubble which is subjected to an impulse force is given by:

$$f = \frac{1}{2\pi r}\left(\frac{3\gamma p}{\rho}\right)^{0.5} \qquad (12)$$

Where r is the bubble radius and, γ is the polytrophic coefficient of the fluid, and r is the bubble radius.

2.2.2 Laboratory Experimentations
Hattori *et al.*, [9], have conducted experiments to investigate the influence of air entrainment on impact pressures from a wave impinging on a vertical solid wall. By varying the wall location relative to the breaking wave they were able to capture and analyse the effects of 4 distinct geometries of the breaking wave. High speed video recording at the impact interface was captured, from which still images were provided. The first generated wave broke against the wall while exhibiting flip-through behaviour without the entrainment of bubbles and thus no oscillatory effects in the time-pressure history plot were observed.
The second wave impacted the wall while having developed a vertically flat wave front. This type of breaker yielded a very high impact pressure $p_{max}/\rho g H_b = 109.6$ followed by a series of high frequency (1 kHz) oscillations which decayed rapidly.
The third type of breaking wave geometry analysed was that of a plunging breaker with a thin lens of air trapped at the interface. Again, high amplitude impulse pressures were recorded, $p_{max}/\rho g H_b = 51.9$ with oscillating frequency 250 Hz.
The final wave profile investigated was that of a plunging breaker with a large trapped air bubble. It was found that the increase in the diameter *l*, of the entrained bubble resulted in a decrease in both the peak impulse pressure and an associated decrease in the oscillating pressure frequencies recorded. The relationship between the bubble diameter and peak pressure, and also the bubble diameter and pressure oscillation frequency was found to vary inversely. Hattori *et al.*, [9], noted that the expression for the oscillating pressure frequency is approximated by:

$$f_{ap} = 180\,(2r)^{-0.5} \qquad (13)$$

3. NUMERICAL MODEL

3.1 Geometry and Boundary Conditions
The simulation set-up is in the configuration of a dam break flow test case as shown on Figure 1 below. The numerical wave tank is 0.3m long and 0.2m high. The tank contains a column of water of width 0.05715m and height 0.01143m. A no-slip boundary condition is prescribed at the tank base and at the vertical walls. As the top of the tank is considered to be open to the atmosphere, the inflow and outflow of fluid is permitted across this boundary. Thus, at this edge a combination of boundary conditions are specified for the pressure and velocity terms of the fluid flow governing equations to model inflow and outflow behaviour whilst maintaining the PIMPLE algorithm stability. In the case of the incompressible model a `fixedValue` boundary condition with a value of zero is specified for the pressure term whilst a `pressureInletOutletVelocity` boundary condition is applied to the velocity term at the top edge boundary of the tank. In the case of the compressible simulation, the numerical value of the

`fixedValue` boundary condition is set to atmospheric pressure conditions (101 kPa) across the edge which represents the top of the numerical tank. The velocity boundary condition is unchanged from the incompressible case. Pressure is sampled at point P1 on the impact interface where the right hand side wall meets the tank base, (see Figure 1).
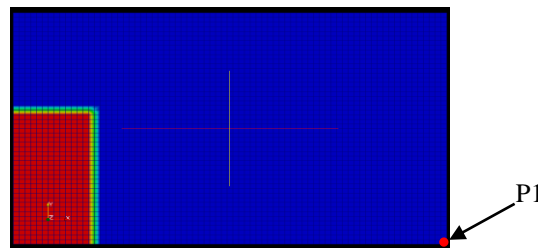

Figure 1: Initial CFD OpenFOAM model setup with
4mm mesh resolution and sampling point P1 indicated.

### 3.2 Flow Profile and Pressure Field Evolution

As the flow simulation progresses, the water column collapses and the flow front advances towards the right hand side (RHS) of the tank. The flow front impacts the solid RHS wall and is forced vertically upwards through the formation of a thin jet. Figure 2(a) and 2(d) present the α function and pressure distribution respectively as the flow front impacts the wall. This initial impact produces the first pressure peak shown on Figure 6(a) in Section 4.3.1 at time t = 0.205. As the jet collapses and converges with the fluid below, a bubble is entrained in the flow. This occurs at t = 0.492 seconds and yields the first oscillatory cycle local minimum pressure shown on Figure 6(b). The free surface geometry at bubble entrainment is displayed on Figure 2(b) with the associated pressure distribution shown on Figure 2(e).
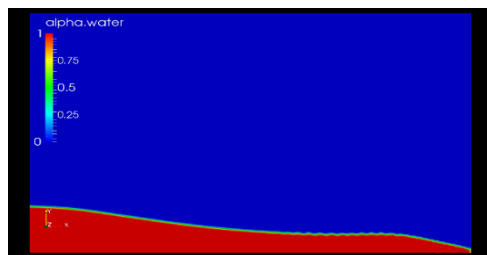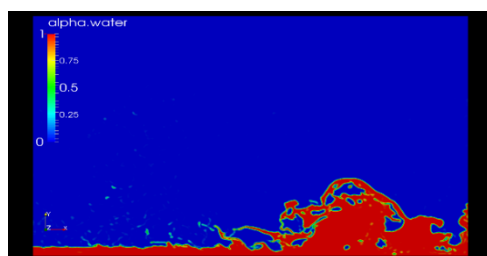

a. Free surface profile at t = 0.205 sec
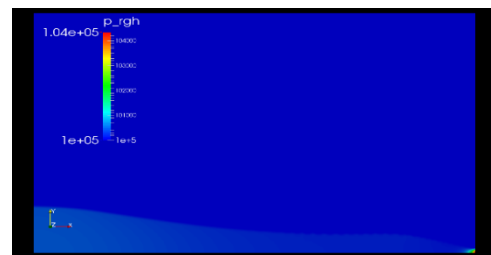
d. Pressure distribution at t = 0.205 sec
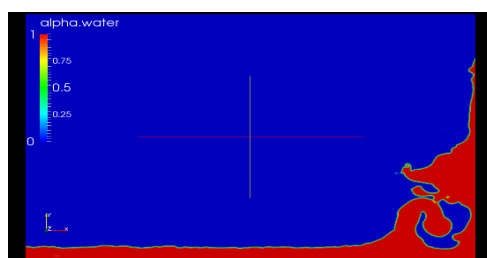
b. Free surface profile at t = 0.492 sec

e. Pressure distribution at t = 0.492 sec

c. Free surface profile at t = 0.610 sec

f. Pressure distribution at t = 0.610 sec

Figure 2: Free surface evolution and associated pressure contour distributions from second
order spatial and second order temporal equation discretisation scheme simulation

The amplitude of the oscillating pressure signal decays in an under-damped manner until the oscillations become negligible at approximately t = 0.610 seconds as presented on Figure 6(b). Figure 2(c) and 2(f) above, display the α function and pressure distribution at time t = 0.610 seconds respectively.

3.3 Spatial and Temporal Domain Discretisation
The spatial domain was initially discretised using a structured 4mm square hexahedral mesh. The mesh resolution was refined three times as part of the grid independence study. Table 1 records the grid resolutions and associated model properties for this section of the study.

Initial simulations were conducted using a specified maximum Courant number of 1.0 and time-step length of 0.00001 sec. For the first order time and spatial discretisation schemes with low level grid resolution this time-step duration was sufficiently short to allow the Courant value to be maintained below 1.0, thus ensuring stability. However as the grid was progressively refined and higher order temporal and spatial equation discretisation schemes were applied to the model, an adaptive time-step control command reduced the time-step duration to ensure convergence of the solution.

Table 1: Grid resolutions

Grid	Δx [mm]	Δy [mm]	No. of nodes	No. of nodes x direction	No. of nodes y direction	No. of elements	No. of elements in x direction	No. of elements in y direction
1	4	4	7752	152	102	3750	75	50
2	2	2	30502	302	202	15000	150	100
3	1	1	121002	602	402	60000	300	200
4	0.5	0.5	482002	1202	802	240000	600	400

4. NUMERICAL SIMULATION RESULTS

4.1 Modelling Scalability Criteria
The grid independence study was established using the grid resolution data from Table 1. The spatial discretisation analysis was performed by calculating the impulse force *I*, at initial wave impact for each level of refinement. The impulse force was obtained for each grid resolution by integrating the maximum impact pressure peak over the rise time [10]:

$$I(x) = \int_{Rt} p(x,t)dt \qquad (14)$$

The duration of impact, which for this study is recorded as the peak rise time measured from a baseline time of 0.19 seconds was determined for each of the four levels of mesh discretisation as shown on Figure 3(a). The impulse force results were then compared to verify that progressive mesh refinement produced a solution trending towards convergence as shown in Figure 3(b). Table 2 records the results from the grid independence study.
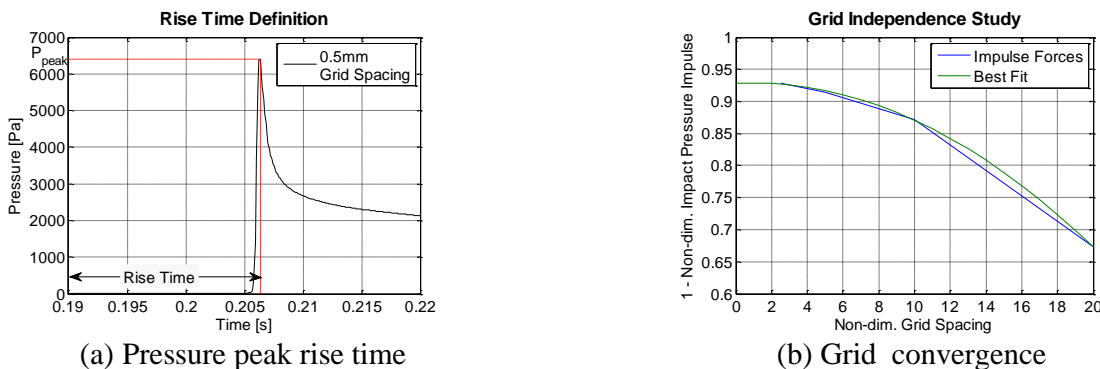

| (a) Pressure peak rise time | (b) Grid convergence |

Figure 3: Model verification (a) pressure peak rise time, (b) grid convergence.

Table 2: Grid independence criteria

Grid	Rise time [R_t] [s]	Non-Dim. Rise time [R_{tnd}]	Peak pressure [p_{max}] [pa]	Non-Dim. Peak pressure [p_{maxnd}]	Non-Dim. impact pressure impulse [p_{ipnd}]
1	0.0233	0.8634	2484.8	2.2160	0.3276
2	0.0170	0.6300	3105.9	2.7700	0.1283
3	0.0169	0.6263	4259.7	3.7990	0.0852
4	0.0163	0.6040	6402.7	5.7102	0.0717

4.2 Model Validation

4.2.1 Collapsing fluid column leading edge position

Numerical model validation was achieved through comparison of the time varying leading edge position of the collapsing fluid column with experimental results from a study performed by Martin and Moyce, [18]. The surge front location for the numerical simulation was plotted for each of the four levels of grid resolution. The results are shown on Figure 4. The flow front position shows good agreement between the different mesh resolution models. The 4mm grid spacing simulation reaches the impact interface later than the higher resolution grid simulations (indicated by a sharp change in derivative of the graphs). This is supported by the rise time data presented in Table 2. Also included on Figure 4 is a plot of the flow front leading edge position sampled during experiment 5 conducted by Martin and Moyce, [18]. The numerical simulation shows good agreement with the experimental results.
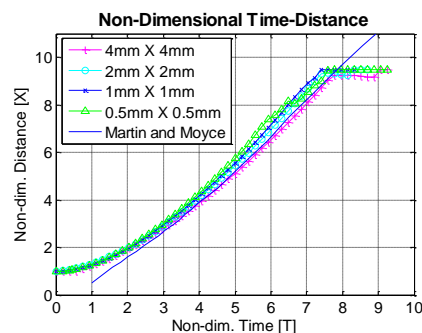

Figure 4: Model validation, flow front position

4.2.2 Transient pressure response comparison

The CFD model is further validated through comparison of the simulation pressure signal results with data from an experimental dam-break study published by Kleefsman *et al.*, [19].
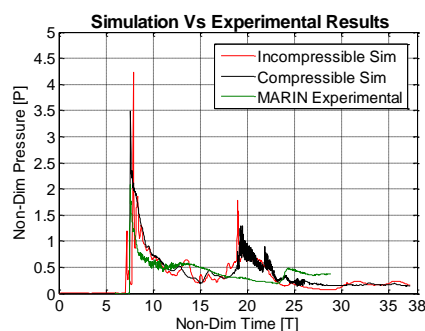

Figure 5: Model validation, transient pressure comparison with experimental results

The geometrical set up for the experiment consisted of a 1.22 metre wide by 0.55 metre high water column which, when released, impacted an obstacle located 1.77 metres from the nearside of the water column. This obstacle measured 0.16 metres wide and 0.16 meter high. By non-dimensionalising the time and pressure response values from the numerical study a direct comparison with the experimental pressure history plots could be made. Figure 5 above, displays a plot of the experimental time pressure

history results from the study published by Kleefsman *et al*., [19], versus both the incompressible and the compressible numerical simulation results. The pressure signal trend shows good agreement between the experimental and numerical results.

4.3 Simulation Pressure Response Results
The series of simulations performed can be classified according to those in which air compressibility effects were neglected and those in which air was considered as a compressible fluid and also according to the temporal and spatial equation discretisation schemes employed. The second order temporal and spatial scheme results are discussed in Section 4.3.1. Some further discussion on the first order temporal and spatial discretisation results for the 1 mm square grid size resolution for both incompressible and compressible simulations follows in Section 4.3.2.

4.3.1 Second order temporal second order spatial equation discretisation scheme
Figure 2 (Section 3.2) displays the α function and pressure distribution as the flow develops during the simulation. The pressure variation as a function of time for both the incompressible air phase simulation and the compressible air phase simulation is shown on Figure 6 below.
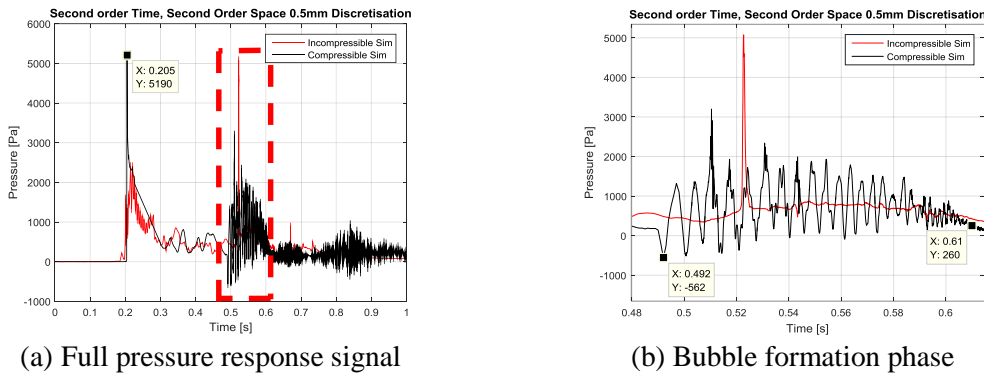
(a) Full pressure response signal   (b) Bubble formation phase
Figure 6: Pressure response signal at P1: (a) Full simulation,
(b) Oscillation due to air entrainment

It can be observed that between t = 0.492 and t = 0.610 a high amplitude, high frequency, resonant oscillation is recorded in the compressible simulation pressure response at point P1. This is due to the entrapment of a large air bubble which occurs as the vertical jet collapses. The initial entrained air bubble has a cross sectional area of approximately 1324.5 mm^2 which results in an equivalent spherical bubble of approximate radius 20 mm. As the simulation progresses this bubble fragments several times to form smaller bubbles. From Figure 6(b) the pressure signal recorded at P1 can be seen to oscillate with a regular frequency. By applying a Fast Fourier Transform (FFT) to the signal, five principal oscillating frequencies of 150, 180, 200, 219 and 252 Hz were computed. Table 3 summarises the formation of the first 5 bubbles observed during the simulation together with the main oscillatory frequencies.

Table 3: Entrained bubble evolvement and associated frequencies

Bubble	Area [mm]^2	Equivalent radius [mm]	Time which bubble forms [sec]	Time which bubble size is modified [sec]	Lifespan of bubble [sec]	Oscillation frequency [Hz]
1	1324.5	20	0.492	0.5045	0.0125	150
2	787	15.8	0.5045	0.5131	0.0086	180
3	474	12.3	0.5045	0.5231	0.0126	200
4	483	12.4	0.5131	0.5341	0.0210	219
5	489	12.5	0.5231	0.5431	0.0260	252

These frequencies can be compared with the adiabatic Minnaert resonant frequency [13], given by Equation (12) and also with the experimentally derived relationship observed by Hattori *et al*., [9], (Equation (13)). These results are presented on Figure 8.
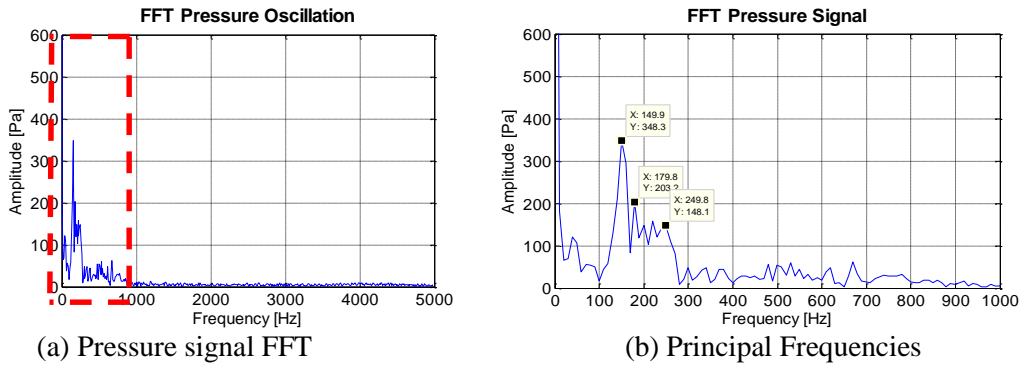
(a) Pressure signal FFT   (b) Principal Frequencies

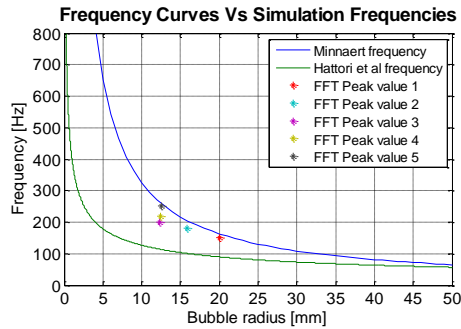**Figure 7: FFT Analysis of pressure oscillation.**

**Figure 8: Analytic & Experimental bubble oscillatory frequencies
versus numerical model frequency predictions**

4.3.2 First order temporal, first order spatial equation discretisation scheme

To further ascertain that the resonant pressure signal oscillations observed at P1 originate from the pulsation of the entrained bubble, analysis was performed on the pressures sampled at a point within the entrapped air bubble.
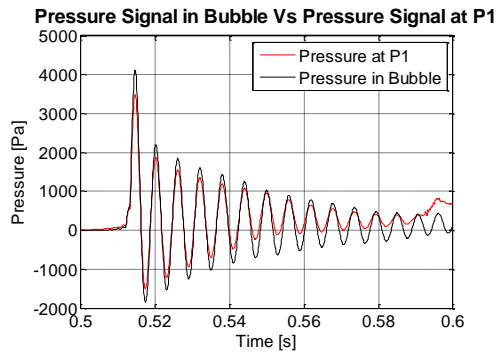

Figure 9: Pressure oscillations at the entrained air bubble vs pressure oscillations at P1

Figure 9 shows the pressure signal inside the air bubble and at position P1 obtained employing the first order temporal and spatial equation discretisation schemes on a 1mm square grid resolution from 0.5 to 0.6 seconds elapsed simulation time. The amplitude of the oscillating pressure signal sampled within the bubble is consistently larger than the pressure recorded at P1. This would imply that the resonant contraction and expansion action of the entrapped bubble is the source of the pressure oscillation. The reduced amplitude of the pressure signal at P1 may be due to energy loss through the free surface and energy loss due to viscous effects within the liquid phase. The pressure oscillation within the bubble also persists for some time after the oscillations at P1 are damped, further supporting the argument that the oscillations emanate from the entrained bubble.

5. CONCLUSIONS AND FUTURE DEVEOPMENTS

The origins of the oscillatory nature of impact pressures at solid walls have been investigated. There is-

clear evidence that the oscillation of the impact pressure at a solid wall is generated from entrapped oscillating air bubbles within the flow. A good size range of entrapped bubbles at the interface with the solid is numerically revealed together with their respective resonant frequencies. The evidenced bubbles respective life spans are found to be finite. One therefore expects the range of bubbles oscillatory frequencies to vary in time as the overall energy of the flow and impact pressures at the wall recede. Further studies of these effects are currently in progress while being applied to complex porous structures. The aim is to quantify the response of the flow at impact at such porous structures together with the manifested oscillatory frequencies of entrapped bubbles as a result.

REFERENCES

1. Topliss, M., Cooker, M., & Peregrine, D. (2011). Pressure oscillations during wave impact on vertical walls. *Coastal Engineering Proceedings, 1*(23).
2. Bullock GN, Obhrai C, Müller G, Wolters G, Peregrine DH and Bredmose H. 2005, Advances in the understanding of wave-impact forces. Int. Conf. on Coastlines, struct. and breakwaters, 111-120
3. Bullock GN, Obhrai C, Peregrine DH and Bredmose H (2007) Violent breaking wave impacts. Part 1: Results from large-scale regular wave tests on vertical and sloping walls. Coastal Engineering 54(8): 602-617
4. Bredmose H, Peregrine DH and Bullock GN (2009) Violent breaking wave impacts. Part 2: Modelling the effect of air. *Journal of Fluid Mechanics* 641: 389-430
5. Oumeraci H, Klammer P and Partenscky HW (1993) Classification of Breaking Wave Loads on Vertical Structures. *J Waterw Port C-Asce* 119(4): 381-397
6. Wemmenhove R, Luppes R, Veldman AEP and Bunnik T (2015) Numerical simulation of hydrodynamic wave loading by a compressible two-phase flow method. *Comput Fluids* 114: 218-231
7. Alagan Chella M, Bihs H and Myrhaug D (2015) Characteristics and profile asymmetry properties of waves breaking over an impermeable submerged reef. *Coastal Engineering* 100: 26-36
8. Bagnold RA (1939) INTERIM REPORT ON WAVE-PRESSURE RESEARCH. (INCLUDES PLATES AND PHOTOGRAPHS). *Journal of the Institution of Civil Engineers* 12(7): 202-226
9. Hattori M, Arami A and Yui T (1994) Wave Impact Pressure on Vertical Walls under Breaking Waves of Various Types. *Coastal Engineering* 22(1-2): 79-114
10. Peregrine DH (2003) WATER-WAVE IMPACT ON WALLS. *Annual Review of Fluid Mechanics* 35(1): 23-43
11. Stagonas D, Marzeddu A, Cobos FXGI, Conejo AS-A and Muller G (2016) Measuring wave impact induced pressures with a pressure mapping system. *Coastal Engineering* 112: 44-56
12. Chan ES and Melville WK (1988) Deep-Water Plunging Wave Pressures on a Vertical Plane Wall. *Proceedings of the Royal Society of London A: Mathematical, Physical and Engineering Sciences* 417(1852): 95-131
13. Minnaert M (1933) XVI. On musical air-bubbles and the sounds of running water. *The London, Edinburgh, and Dublin Philosophical Magazine and Journal of Science* 16(104): 235-248
14. The Openfoam Foundation (2013) The Open Source CFD Toolbox, User Guide & Programmer Guide.
15. Hirt CW and Nichols BD (1981) Volume of Fluid (Vof) Method for the Dynamics of Free Boundaries. *J Comput Phys* 39(1): 201-225
16. Sabeur ZA, Roberts W and Cooper AJ (1995) Development and Use of an Advanced Numerical Model using the VOF Method for the Design of Coastal Structures. IN: Morton KW and Baines MJ (eds) *Numerical Methods for Fluid Dynamics V*: Oxford University Press 565-573
17. Martínez Ferrer PJ, Causon DM, Qian L, Mingham CG and Ma ZH (2016) A multi-region coupling scheme for compressible and incompressible flow solvers for two-phase flow in a numerical wave tank. *Computers & Fluids* 125: 116-129
18. Martin JC and Moyce WJ (1952) Part IV. An Experimental Study of the Collapse of Liquid Columns on a Rigid Horizontal Plane. *Philosophical Transactions of the Royal Society of London A: Mathematical, Physical and Engineering Sciences* 244(882): 312-324
19. Kleefsman KMT, Fekken G, Veldman AEP, Iwanowski B and Buchner B (2005) A Volume-of-Fluid based simulation method for wave impact problems. *J Comput Phys* 206(1): 363-393

ACKNOWLEDGEMENT